# 4 Oscillators with Elastic Contact and Friction

To verify the developed point contact model with friction, a comparison of measurements and calculations with respect to the normal and tangential contact behavior is carried out. The experimental setup, shown in Fig. 3.6-1, is used for the investigations in the normal and tangential directions, see also (Hinrichs et al. 1997b, 1998). On the one hand, an oscillator with an elastic normal contact and on the other hand a self-excited oscillator with friction is analyzed. The theoretical foundation for both investigated systems is derived in a more general sense within the next Chapter. Due to the strong non-linearity of the normal and tangential contact, the systems are analyzed in the time domain.

## 4.1 System Description

In **Fig. 4.1-1**, the investigated system model with $n$ possible contact points at the surface of an elastic body is depicted. The body is assumed linear elastic, as described in Chapter 2. The surface of the elastic body, where contact can occur, is discretized and for each possible contact node, the contact and friction laws have to be formulated. The ground is moving with the constant velocity $V$. The normal force $F_{Nj}$ and the tangential force $F_{Rj}$ act at the node $j$.

The vibration amplitudes of the elastic body, the external forces and the contact forces are described in the initial $I$-coordinate-system. With respect to the elastic body, the excitation point $B$ is introduced, where two external loads and one external moment are applied. A constant force $F_{N0}$ like the gravity force is applied at the node $C$ parallel to the ${}_I y$-axis. The surface at the node $j$ is defined by the height $y_{Rj}$. As derived in Chapter 2.4, the dynamics are given by the equation of motion

$$\boldsymbol{diag}(\ddot{q}_i + 2\omega_{0i} D_i \dot{q}_i + \omega_{0i}^2 q_i) = \boldsymbol{T}^T \boldsymbol{f}_{ex} = \boldsymbol{R} \,. \tag{4.1-1}$$

The transformation into the state space requires the definition of the state vector,

$$\boldsymbol{y} = \begin{bmatrix} q_1 & \dot{q}_1 & q_2 & \dot{q}_2 & \cdots & q_m & \dot{q}_m \end{bmatrix}^T , \tag{4.1-2}$$

with the number $m$ of modes. Hence, differential equation of second order defined in Eq.(4.1-1) can be transferred to a set of differential equation of first order

$$\begin{aligned} \dot{y}_{2i-1} &= y_{2i}, \\ \dot{y}_{2i} &= -2\omega_{0i} D_i y_{2i} + \omega_{0i}^2 y_{2i-1} + R_i. \end{aligned} \tag{4.1-3}$$

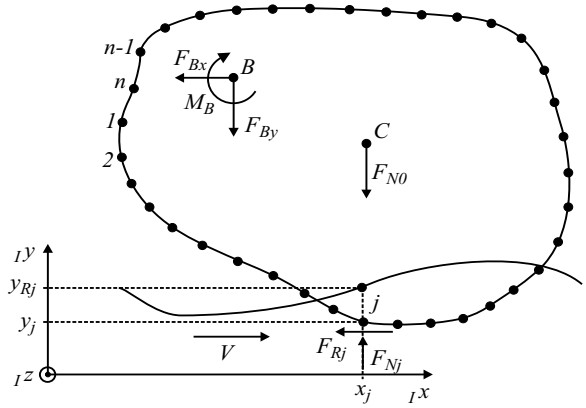


**Fig. 4.1-1** Elastic body with friction contacts

Here, the external force vector of the elastic body is defined by

$$\boldsymbol{f}_{ex} = \left[\boldsymbol{F}_B^T \quad \boldsymbol{F}_C^T \quad \boldsymbol{F}_1^T \quad \boldsymbol{F}_2^T \quad \ldots \quad \boldsymbol{F}_j^T \quad \ldots \quad \boldsymbol{F}_n^T\right]^T \tag{4.1-4}$$

with the generalized forces

$$\boldsymbol{F}_B = \left[-F_{Bx} \quad -F_{By} \quad -M_B\right]^T, \tag{4.1-5}$$

$$\boldsymbol{F}_C = \left[0 \quad -F_{N0} \quad 0\right]^T \tag{4.1-6}$$

and the generalized contact forces at the node *j*

$$\boldsymbol{F}_j = \left[-F_{Rj} \quad F_{Nj} \quad 0\right]^T. \tag{4.1-7}$$

The points *B* and *0* are connected by springs in the *x*- and *y*-direction, which are not shown in Fig. 4.1-1. Furthermore, absolute viscous damping with respect to the point *B* is assumed. Then, the external forces of the elastic body are given by

$$F_{Bx} = c_x(x_B - u_{0x}) + b_x\dot{x}_B, \tag{4.1-8}$$

$$F_{By} = c_y(y_B - u_{0y}) + b_y\dot{y}_B \tag{4.1-9}$$

and $M_B=0$, where the point *0* is harmonically excited with

$$u_{0x}(t) = x_0\sin(\omega_E t) \tag{4.1-10}$$

and

$$u_{0y}(t) = y_0\sin(\omega_E t). \tag{4.1-11}$$

Using the modal description of the linear elastic body, the generalized displacement vector of the elastic body is given by

$$\boldsymbol{w} = \boldsymbol{T}\boldsymbol{q} \tag{4.1-12}$$

with

$$\boldsymbol{w} = \left[x_B \quad y_B \quad \varphi_B \quad x_C \quad y_C \quad \varphi_C \quad x_1 \quad y_1 \quad \varphi_1 \quad \ldots\right]^T \tag{4.1-13}$$

and the generalized velocity vector

$$\boldsymbol{v} = \boldsymbol{T}\dot{\boldsymbol{q}} \tag{4.1-14}$$

with

$$\boldsymbol{v} = \left[\dot{x}_B \quad \dot{y}_B \quad \dot{\varphi}_B \quad \dot{x}_C \quad \dot{y}_C \quad \dot{\varphi}_C \quad \dot{x}_1 \quad \dot{y}_1 \quad \dot{\varphi}_1 \quad \ldots\right]^T. \tag{4.1-15}$$

The normal contact force with respect to the node *j* is given by Eq.(3.2-24)

$$F_{Nj} = c_{N0\,j} R_{Zj} f^*(u^*_{Nj}) + \beta_j c_{N0\,j} h^*(u^*_{Nj}) v_{Nj} \geq 0\,. \tag{4.1-16}$$

The relative normal penetration is given by

$$u_{Nj} = y_{Rj} - y_j\,, \tag{4.1-17}$$

where $y_{Rj}$ denotes the macroscopic displacement of the moving ground like the waviness. Then, the corresponding velocity in the ${}_Iy$-direction normal to the ground velocity $V$ is given by

$$v_{Nj} = \dot{u}_{Nj} = \dot{y}_{Rj} - \dot{y}_j\,. \tag{4.1-18}$$

The relative tangential displacement and velocity of each contact element is given by

$$u_{rj} = x_j - Vt \tag{4.1-19}$$

and

$$v_{rj} = \dot{u}_{rj} = \dot{x}_j - V, \tag{4.1-20}$$

respectively.

To reduce the degrees of freedom of the investigated system and, hence, to reduce the computation time, the tangential contact elasticity is modeled as a part of the elastic body. The contact stiffness due to the contact model, described in Chap. 3.3 is then assumed to be infinite.

Assuming dry friction the friction force at the node *j* is given by

$$F_{Rj} = \mu(v_{rj}) F_{Nj}\; s(v_{rj}) \tag{4.1-21}$$

with the friction coefficient $\mu$, which is assumed to be nonlinearly dependent on the relative velocity $v_{rj}$ with

$$\mu(v_{rj}) = (\mu_0 - \mu_\infty) e^{-\lambda_e \left| v_{rj} \right|} + \mu_\infty\,, \tag{4.1-22}$$

with a decreasing characteristic for $\lambda_e > 0$ and the smoothing function

$$s(v_{rj}) = \frac{2}{\pi} \arctan(k_S v_{rj})\,, \tag{4.1-23}$$

with the slope parameter $k_S$, which defines the slope at zero relative velocity $v_{rj}=0$. For large slope parameters $k_S$, the non-smooth system dynamics can be approximated. A disadvantage due to large values of this slope parameter is the occurrence of stiff differential equations. But there exist numerical integration methods with variable step size, which calculate the numerical or, if available, use the analytical Jacobian matrix of the investigated system, see for example (NAG 1986) and (SIMULINK 1999). Both improvements speed up the solution procedure and solve the system equations for relatively large values of the slope parameter in a reasonable time and an acceptable accuracy. Due to the investigations with respect to the relative error, see Chapter 3.7 and Fig. 3.7-3, the slope parameter is set to be $k_S = 10^6$ [*s/m*] in the following.

## 4.2 Oscillator with Elastic Contact

The experimental setup is shown in Fig. 3.6-1, where a pendulum supported by springs represents the linear oscillator. The rotational degree of freedom of the pendulum and its degree of freedom normal to the plane of rotation have been realized by air bearings providing small damping. A magnetic excitation force realizes the harmonic excitation, see (Popp et al. 1996). For the experimental investigation of the impact oscillator, the pendulum hits a stop. A more detailed description of the test stand is given in (Hinrichs et al. 1997b). The reduced system parameters of the oscillator shown in Figure 4.2-1 are given by: $m=0.092$ $[kg]$, $c_y=99.085$ $[N/m]$, $b_y=0.02046$ $[Ns/m]$, $y_0=0.00047$ $[m]$, $y_R=0.0$. The contact law is defined by Eq.(4.1-16), where the following contact parameter have been used: $c_{N0}=0.3\ 10^6$ $[N/m]$, $R_Z=5.2$ $[\mu m]$, $\beta c_{N0}=6.0$ $[Ns/m]$. Additionally, the modal parameters of the first bending mode of the pendulum, see Figure 3.6-1, have been estimated by the simple beam theory.

The model investigated is shown in **Fig. 4.2-1**, which is excited by a harmonic displacement of the point *0*. The contact parameters and relative displacements and velocities are assumed to be constant within the contact region. Then, the system response to the harmonic excitation is independent on the number $n$ of contact elements and, hence, the number of contact points can be reduced to one. Here, the error with respect to the discretization of the contact area is identical to zero.

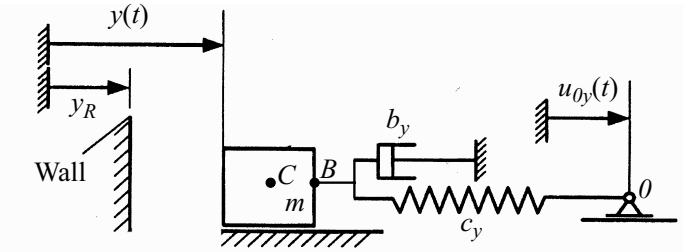


**Fig. 4.2-1** Oscillator with elastic contact

In **Fig. 4.2-2**, the comparison of the measurements and calculation of phase diagrams for different excitation angular frequencies $\omega_E$ are shown. If the displacement $y$ is less than $y_R=0.0$, the elastic body contacts the wall, see **Fig. 4.2-2a** and **b**. The influence of the higher modes is quite high just after the elastic contact, when separation takes place.

The comparison is good as well for period two oscillations, compare **Fig. 4.2-2c** with **d**, and for higher periodic oscillations, compare **Fig. 4.2-2e** and **f** as well as for chaotic motions, compare **Fig. 4.2-2g** with **h**. Overall, modeling the elasticity of the contact and the higher modes of the elastic body is an extension and an improvement compared to a non-smooth description of the contact law combined with the rigid body formulation, see (Hinrichs et al. 1998).

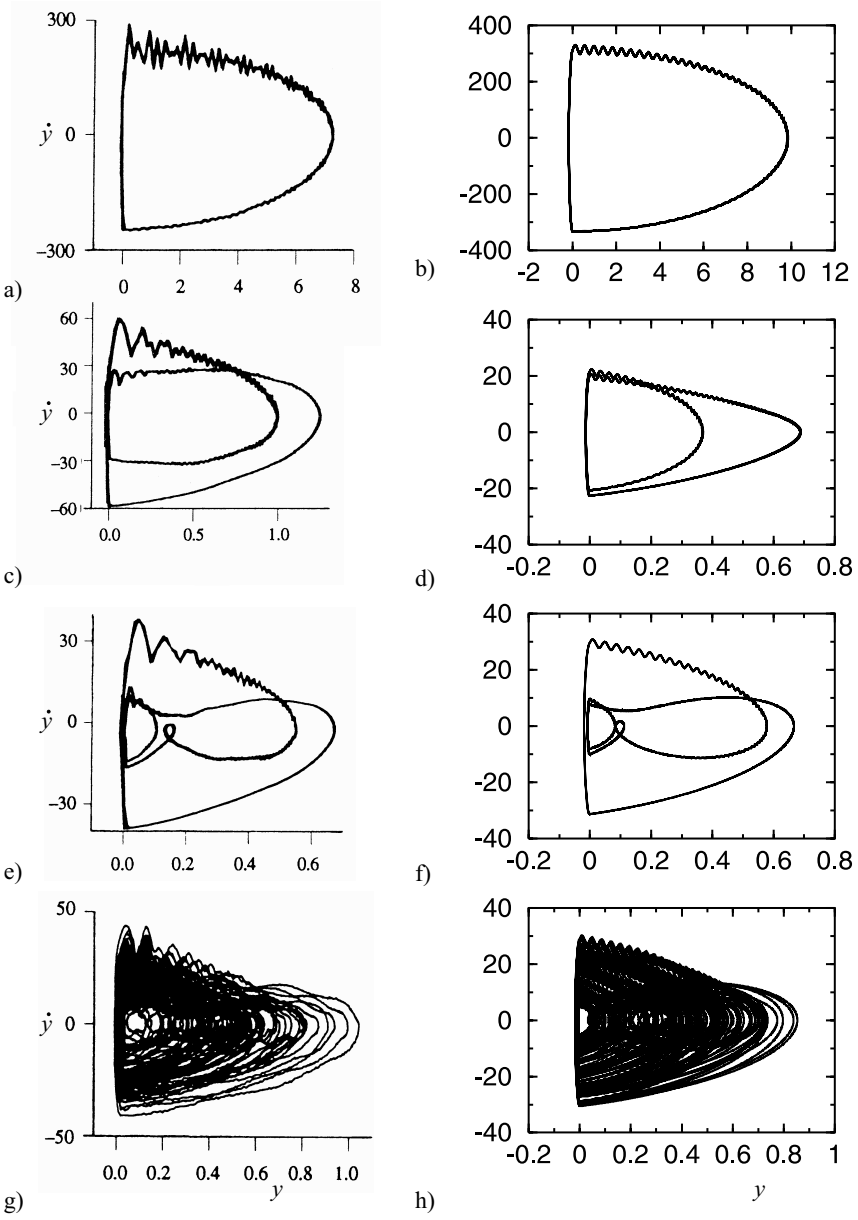


**Fig. 4.2-2** Phase diagrams of measurements (Hinrichs 1997b) and calculations for different excitation angular frequencies $\omega_E$ **a**) measurement and **b**) calculation for $\omega_E$=*64.32* [*rad/s*] **c**) measurement and **d**) calculation for $\omega_E$=*30.84* [*rad/s*] **e**) measurement and **f**) calculation for $\omega_E$=*37.41* [*rad/s*] **g**) measurement and **h**) calculation for $\omega_E$=*23.63* [*rad/s*]

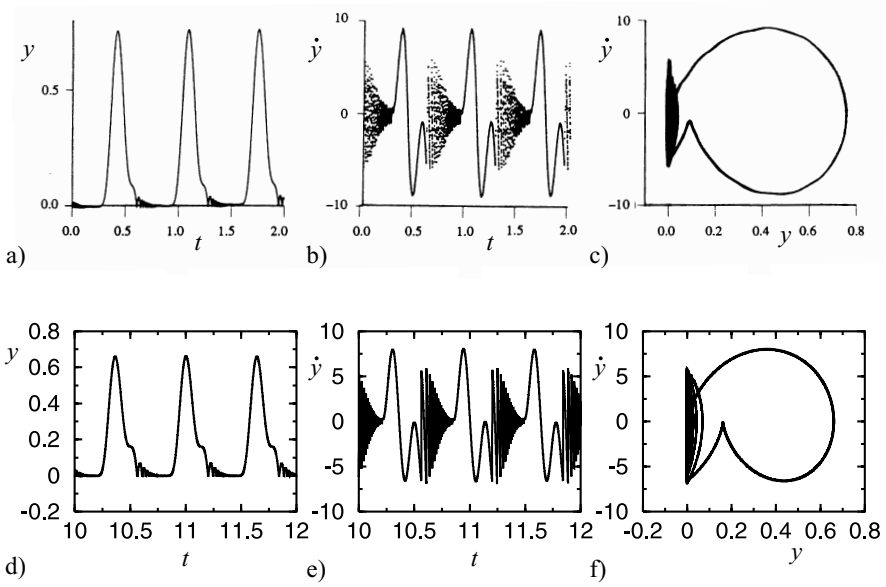


**Fig. 4.2-3** Comparison of measurements (Hinrichs 1997b) and calculations for the excitation angular frequencies $\omega_E$=*9.845* [*rad/s*] **a**) measurement of displacement and **b**) velocity **c**) measured phase plot **d**) calculation of displacement and **e**) velocity **f**) calculated phase plot

In **Fig. 4.2-3**, a phenomenon is studied which is called chatter. The rebouncing of the oscillator leads to sticking at the stop for an infinite number of elastic contacts. Furthermore, the calculated displacements, velocities and phase plots are compared with the corresponding measurements. In this extreme example, the agreement of measurements and calculations is also very good.

## 4.3 Friction Oscillator

The experimental setup is shown in Fig. 3.6-1 again and is modified with respect to the friction contact. The pendulum is pressed onto the disc driven with constant speed. The real rotational system is reduced to the friction oscillator shown in **Fig. 4.3-1**, where a belt instead of a disc moves with the velocity *V*. The system is excited by a harmonic displacement of the point *0*. The normal contact force $F_{N0}$ is assumed to be constant.

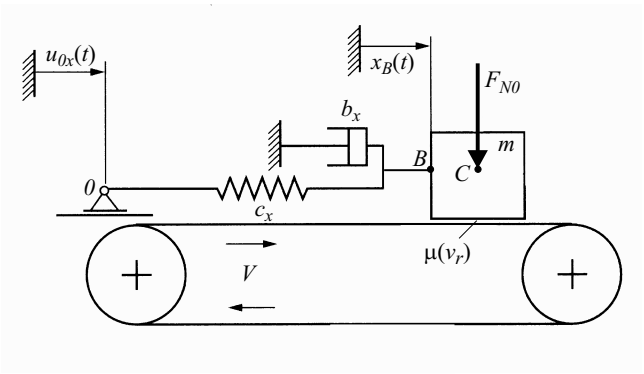


**Fig. 4.3-1** Friction oscillator

To verify the tangential contact model, the measurements presented in (Hinrichs et al. 1998), see **Fig. 4.3-2a**, and the following experimental data are used: $V=0.001$ [$m/s$], $\omega_E=13.8$ [$rad/s$], $F_{N0}=14.0$ [$N$], $x_0=0.0005$ [$m$], $m=5.632$ [$kg$], $c_x=5610.0$ [$N/m$], $b_x=0.768$ [$Ns/m$]. The material contact partners are steel and polyurethane modeled with the following contact parameters: $\mu_0=0.8$, $\mu_\infty=0.55$, $\lambda_e=1000.0$ [$s/m$], $c_{N0}=10.0\ 10^6$ [$N/m$], $R_Z=10.0$ [$\mu m$], $\beta c_{N0}=40.0$ [$Ns/m$]. The error with respect to the discretization is again zero, because only translations of the mass are involved. For a given normal contact force, the static normal displacement has to be calculated iteratively, because the normal force is nonlinearly dependent on the relative normal displacement by Eq.(4.1-16). This iteration can be omitted, if the first rigid body mode in the normal direction is included within the model of the elastic body. The rigid body mode of the mass in the tangential direction results in a one-periodic solution shown in **Fig. 4.3-2b**. Including the elasticity of the higher mode leads to an improvement of the calculations, see **Fig. 4.3-2c**, which shows oscillations with higher frequency after the transition from slip to stick. The modal parameters for this higher mode have been approximated by the data given in (Hinrichs 1997a). However, the calculations do not show the measured high-periodic oscillations. Hinrichs (1997a) explained this phenomenon with a stochastic varying friction coefficient.

A further reason for this physical effect can be the surface profile. Besides the roughness, the waviness of the contact surface can influence the dynamical behavior. Assuming that the waviness of the ground is dominated by a single sine wave, the displacement in the $y$-direction at the node $j$ is given by

$$y_{Rj} = y_A \sin\left(2\pi \frac{u_{rj}}{\lambda}\right), \tag{4.3-1}$$

with the wave amplitude $y_A$, the wave length $\lambda$ and the relative displacement $u_{rj}$ given by Eq.(4.1-19). The wave amplitude of $y_A=200.0$ [$\mu m$] and the wave length of $\lambda=2.5$ [$mm$] results in a higher-periodic solution shown in **Fig. 4.3-2d**, which shows a good qualitative and quantitative agreement with the measurement,

shown in Fig. 4.3-2a. A further improvement of the calculation could be to use the wave spectrum of the surface and to expand Eq.(4.3-1) in a Fourier series.

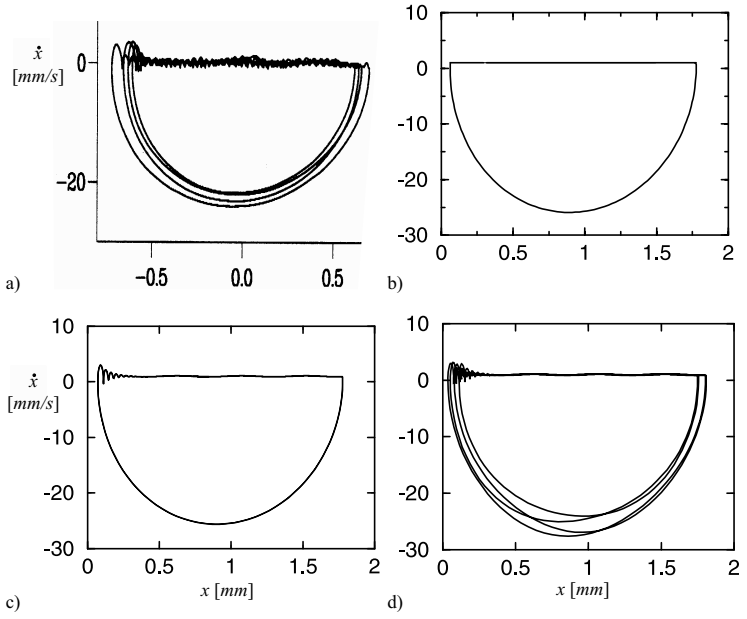


**Fig. 4.3-2** Phase diagrams **a**) measurement (Hinrichs 1997a) **b**) calculation using two modes **c**) three modes **d**) three modes plus modeling waviness

The analysis of systems with dry friction shows a rich dynamic behavior from equilibrium to chaos. Bifurcation scenarios like period doubling sequences are described for example in (Feeny and Moon 1994; Oestreich et al. 1996; Popp et al. 1995a, 1995b, 1996, 2005, Hoffmann 2006).

## 4.4 Bifurcations in Dynamical Systems with Friction

In (Stelter and Sextro 1991) the bifurcation theory described in (Seydel 1983) has been applied to a two degree of freedom system using a smooth friction characteristic. Period doublings and Hopf-bifurcations as well as turning points have been determined. Both, unstable branches and stable coexisting solutions have been calculated. Several jumping effects, which are typical for nonlinear systems, have been found. The mathematical modelling of dry friction forces leads to nonlinear equations of motion. Beside of periodic solutions, more complicated motions are possible. When these motions are generated by deterministic equations, deterministic chaos may occur. The routes to chaos may be via period doublings, torus-bifurcations or intermittency, see (Kreuzer 1987) and (Troger 1991). One aim of

the investigations is to calculate the bifurcations, where the solution changes dramatically. The classification of the bifurcations is possible by the Floquet theory, see (Seydel 1988a) and Iooss (1980). Furthermore, the typical bifurcation scenarios are most important for the understanding of self-sustained oscillations. In order to show the basic phenomena of dynamic systems with dry friction, a simple model of a two mass spring system has been taken in account leading to the following set of equation of motion, see (Stelter 1990) and (Stelter and Sextro 1991)

$$\begin{aligned} x_1' &= x_2 \\ x_2' &= \left[-(1+\kappa)x_1 - 2D(1+\delta)x_2 + x_3 + 2Dx_4 + B\rho\{\mu(x_2=0) - \mu(v_{r1})\}\right] \\ x_3' &= x_4 \\ x_4' &= x_1 + 2Dx_2 - x_3 - 2Dx_4 + B\{\mu(x_4=0) - \mu(v_{r2})\} \end{aligned} \tag{4.4-1}$$

Eq.(4.4-1) represents a two-masses-spring-damper system, which is excited by friction forces exerted by a running band. Self-excitation due to dry friction is only possible when the friction force has a decreasing characteristic, see (Magnus 1976). The parameter dependencies of the solution can be calculated with program package BIFPACK. Furthermore, the bifurcation behaviour can be investigated with the use of the Floquet theory, see (Seydel 1988a), (Hagedorn 1984) and (Iooss 1980). With the Floquet theory a unique classification of the global bifurcations is possible. For generalization the following abbreviations have been introduced: the mass ratio

$$\gamma := m_1 / m_2 , \tag{4.4-2}$$

the damping ratio

$$\delta := d_1 / d_2 , \tag{4.4-3}$$

the stiffness ratio

$$\kappa := c_1 / c_2 , \tag{4.4-4}$$

the normal force ratio

$$\rho := F_{N1} / F_{N2} \tag{4.4-5}$$

and the load parameter

$$B := F_{N2} / c_2 . \tag{4.4-6}$$

The dimensionless damping is given by

$$D := d_2 / 2\sqrt{c_2 m_2} . \tag{4.4-7}$$

The chosen parameter values are

$$\omega_2 = 1.0 s^{-1}, \gamma = 2.5, \delta = 1.0, \kappa = 2.0 \text{ and } \rho = 1.0 .$$

The nonlinear structure of equation (4.4-1) becomes obvious by the vector notation

$$\boldsymbol{x}' = \boldsymbol{A}\boldsymbol{x} + \boldsymbol{r}(\boldsymbol{x}) \tag{4.4-8}$$

where **A** is the linear system matrix and **r** is the vector of the nonlinear friction forces. For the use of the program package BIFPACK developed by Seydel (1988b), the function of friction force has to be continuously differentiable. Thus, for the numerical simulations the following model for the friction characteristic was used

$$F_{Ri} = -F_{Ni}\mu(v_{ri})$$
$$\mu(v_{ri}) = a_1\left(1 + a_2 \exp(-b|v_{ri}|\right)\arctan(b_2 v_{ri}) \qquad (4.4\text{-}9)$$
$$i = 1,2$$

with the constants

$$a_1 = 0.14,\ a_2 = 1.14,\ b_1 = 2.0s/m,\ b_2 = 100.0s/m\,,$$

where $\gamma$ denotes the friction coefficient, which depends on the relative velocity $v_r$, and $F_N$ denotes the normal force. The relative velocities is given by

$$v_{ri} = \omega_2 x'_{2i} - v_0\,. \qquad (4.4\text{-}10)$$

To be able to characterize the solution nearby the equilibrium the Jacobian $\boldsymbol{J}$ has to be calculated by differentiation of Eq.(4.4-8) with regard to $\boldsymbol{x}$.

$$\boldsymbol{J}(\boldsymbol{x}) = \boldsymbol{A} + \frac{\partial \boldsymbol{r}(\boldsymbol{x})}{\partial \boldsymbol{x}} \qquad (4.4\text{-}11)$$

The amplitude $x_3$ has been used to show the bifurcation behaviour. The important parameters of the system are the load parameter $B$, the band velocity $v_0$ and the damping $D$. Within the bifurcation diagrams, Hopf-bifurcations, turning points and period doubling occur, while stationary bifurcations do not appear. To determine the Hopf-bifurcations, one has to calculate the eigenvalues of the Jacobian. They occur when a complex pair crosses the imaginary axis. The equilibrium $\boldsymbol{x=0}$ is stable, when all eigenvalues are within the left side of the complex plane.

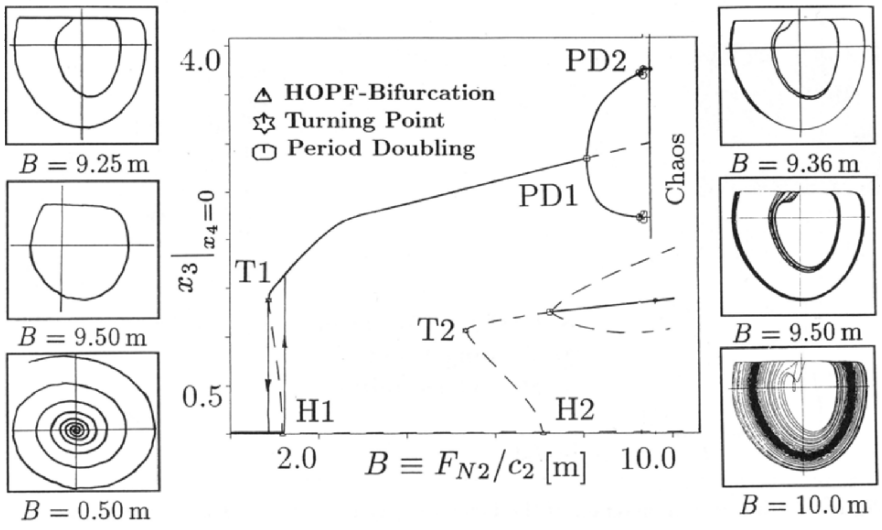


**Fig. 4.4-1** Bifurcation diagram of the load parameter with phase plane plots

In the bifurcation diagram of the load parameter, see **Fig. 4.4-1** a sub-critical Hopf-bifurcation (H1) arises at a parameter value of $B$=1.12 m, while a special Hopf-bifurcation (H2) occurs at $B$=7.09 m. Starting from the equilibrium the amplitude is jumping from the sub-critical Hopf-bifurcation (H1) to the stable periodic branch. On the other hand, coming from the periodic branch, the amplitude is

jumping from the turning point (T1) to the equilibrium. This jumping phenomenon is typical for systems with dry friction. The unstable branch between the turning point and the sub-critical Hopf-bifurcation can be understood as a borderline between the stable attractors. Here, a stable periodic attractor and a stable equilibrium coexist within a parameter range of 0.88 m<$B$<1.12 m. Following the periodic attractors several period doublings occur, which end in a chaotic motion. The calculated period doublings are at the load parameters of 8.09 m, 9.26 m, and 9.36 m. Beside the bifurcation scenario via period doubling a coexisting periodic solution starts at a load parameter of $B$=7.25 m.

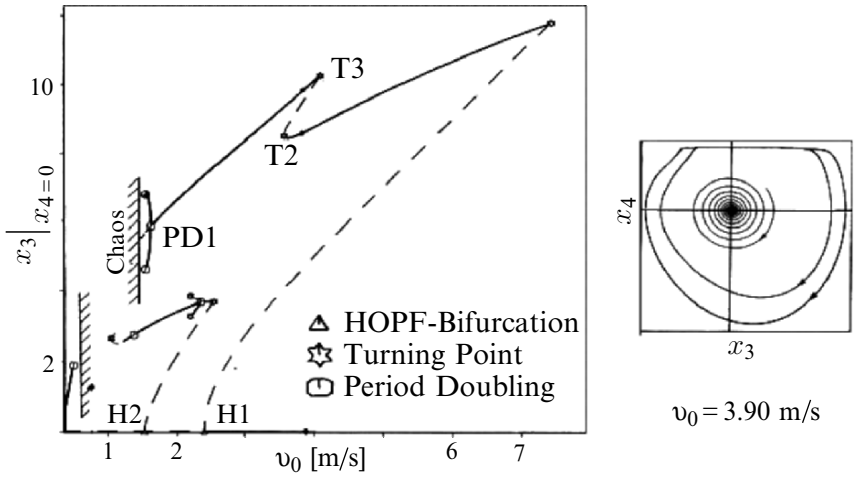


**Fig. 4.4-2** Bifurcation diagram of the band velocity

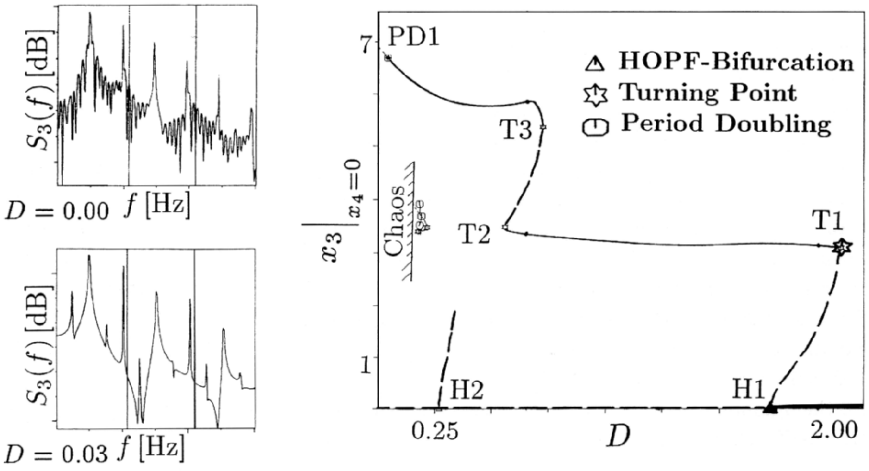


**Fig. 4.4-3** Bifurcation diagram of the damping coefficient

Furthermore the bifurcation diagrams of the band velocity, see **Fig. 4.4-2**, and the damping ratio $D$, see **Fig. 4.4-3**, and have been obtained by means of the program package BIFPACK. They also show turning points, Hopf-bifurcations and period doublings. The routes to chaos are also via period doublings. Coexisting solutions, which are limited by sub-critical period doublings and turning points, could be determined. In Fig. 4.4-2, three stable attractors coexist within the parameter range of 3.57 m/s < $v_0$ < 4.09 m/s.